MIT Libraries | DSpace@MIT

MIT Open Access Articles

Dynamics of Dispersion Managed Octave-Spanning Titanium:Sapphire Lasers

The MIT Faculty has made this article openly available. ***Please share*** how this access benefits you. Your story matters.

Citation: Michelle Y. Sander, Jonathan Birge, Andrew Benedick, Helder M. Crespo, and Franz X. Kärtner, "Dynamics of dispersion managed octave-spanning tiphire lasers," J. Opt. Soc. Am. B 26, 743-749 (2009) tanium:sap

As Published: http://dx.doi.org/10.1364/JOSAB.26.000743

Publisher: Optical Society of America

Persistent URL: http://hdl.handle.net/1721.1/49512

Version: Author's final manuscript: final author's manuscript post peer review, without publisher's formatting or copy editing

Terms of Use: Article is made available in accordance with the publisher's policy and may be subject to US copyright law. Please refer to the publisher's site for terms of use.

Massachusetts Institute of Technology

Dynamics of Dispersion Managed Octave-Spanning Titanium:Sapphire Lasers

Michelle Y. Sander,[1,*] Jonathan Birge,[1] Andrew Benedick,[1] Helder M. Crespo[1,2] and Franz X. Kärtner[1]

[1]*Department of Electrical Engineering and Computer Science and Research Laboratory of Electronics, Massachusetts Institute of Technology, Cambridge, MA, 02139-4307, USA*

[2]*Departamento de Física, Faculdad de Ciências, Universidade do Porto, 4169-007 Porto, Portugal*

[*]*Corresponding author: sanderm@mit.edu*

An extensive one-dimensional laser model based on dispersion managed mode-locking is presented that accurately describes the pulse dynamics of octave-spanning Titanium:sapphire lasers generating sub-two-cycle pulses. By including detailed characteristics for the intracavity elements (mirrors and output coupler), it is demonstrated that the spectral output and temporal pulse shape of these lasers can be predicted quantitatively in very good agreement with experimental results.

© 2008 Optical Society of America

OCIS codes: 140.4050, 140.7090, 320.5550, 320.7090

Introduction

Since the discovery of Kerr-lens mode-locking (KLM) in Titanium:sapphire (TiSa) lasers in 1991 [1], femtosecond mode-locked lasers underwent rapid progress, which led to the generation of octave-spanning lasers with sub-two-cycle optical pulses [2, 3, 4] that also operate at high repetition rates [5]. To better understand the pulse formation in femtosecond mode-locked lasers much advancement in the modelling and understanding of the pulse formation was made: For special cases with small changes per round-trip, analytical solutions of solitary waves with secant hyperbolic functions are formed through the distributed balanced action of self-phase modulation (SPM) and group delay dispersion (GDD). The average dynamics are captured by the Master-equation [6] as a continuous way of describing intracavity effects based on average dispersion values. The importance and limiting effects of dispersion on such solitary systems, especially higher order dispersion, as a perturbative effect on mode-locking were examined in [7, 8, 9, 10]. Alternative approaches that combine temporal and spatial pulse dynamics based on Fresnel integrals were pursued as well [11, 12].

The temporal pulse evolution in Kerr-lens mode-locked Ti:sapphire lasers is well described by dispersion managed mode-locking (DMM) [13, 14]: In systems where the group delay dispersion periodically changes its sign, with small average GDD per round-trip when compared to the absolute GDD in each section (as is the case in femtosecond laser cavities), dispersion managed solitary pulses are formed. Based on the encountered GDD and SPM, together with the localized impact and order of the intracavity elements, the pulses undergo temporal and spectral broadening and recompression during each cavity round-trip [13, 14]. When applied to standard non-octave-spanning mode-locked lasers, simulations based on DMM

have been used to describe their behavior accurately, thus relating pulse energy to pulse duration [15] or including mirror characteristics for detailed output characteristics [16]. Numerical analysis of the spatio-temporal pulse dynamics, in terms of Gaussian beam propagation combined with DMM effects [17], have been compared with analytical results based on the variational principle, including second-order dispersion, self-focusing, diffraction and second-order dispersion of the mirrors [18, 19].

The focus of this work is to extend the one-dimensional model, which describes the temporal dynamics, to include higher order material dispersion as well as the detailed mirror and output coupler characteristics, and to make a quantitative comparison between the DMM model and experimental results from sub-two-cycle, octave-spanning lasers. To our knowledge, the full spectral characteristics of dispersive mirrors and output couplers have never been taken into account to such an extent for sub-two-cycle laser systems. In addition, a comparison between the simulated output pulse and the retrieved pulse from two-dimensional spectral shearing interferometry (2DSI) [20] is performed for the first time. It is shown that the model can capture the octave-spanning output spectrum and the generated sub-two-cycle pulses in great detail, thereby allowing for a direct and precise comparison with experimental measurements. Thus, laser dynamics, stability, and steady-state spectral output can be predicted and optimized based on realistic parameters.

In this paper, we describe the numerical model based on the Nonlinear Schrödinger Equation for the crystal and then derive the different cavity parameters. Next, important intracavity elements and the experimental set-up are explained. In Section 4, the pulse dynamics in steady state for one round-trip are presented. Experimental output spectra for three different

laser cavity configurations and laser parameters are compared with numerical results, and the impact of dispersion compensation and mirror ripples on laser performance is evaluated.

Model

To follow the femtosecond pulse generation in sub-two-cycle, octave-spanning laser systems, we conduct a numerical analysis based on a one-dimensional model and then compare the results with experimental data. We apply this analysis to three different cavity configurations, thus underlining the validity of the chosen approach, and demonstrate its capability to predict important laser characteristics such as pulse duration and shape, bandwidth, and spectral output.

The schematic set-ups of the considered femtosecond laser cavities are given in Fig. 1(a) for a ring and in Fig. 1(c) for a linear laser: In this work, we focus on prismless Ti:sapphire laser cavities that directly generate octave-spanning output spectra at low and high repetition rates [21, 22, 23, 24, 25]. All lasers developed in our group use custom-designed, double-chirped mirror (DCM) pairs, thereby enabling broadband dispersion compensation over almost one octave. For dispersion compensation, either BaF_2 or two wedges of fused silica (FS) and BaF_2 are inserted. To obtain the best agreement with the experimental set-up, the various elements within the cavity are modelled as accurately as possible in terms of their physical characteristics.

The pulse dynamics for any Ti:sapphire laser are determined by the nonlinear propagation through the Ti:sapphire crystal and the linear evolution through the remaining passive cavity elements such as air path, mirrors, output coupler, and wedges. When taking into account the discrete impact, spatial location, and order of each intracavity element, the temporal evolution of the pulse and its spectral envelope for the cavity position z can be followed. Within the crystal, the pulse dynamics are described by Eq. (1), the Nonlinear Schrödinger Equation (NLS, [26]): During each pass through the crystal, the pulse encounters gain saturation together

with Lorentzian filtering *g(z, t)*, dispersion of the Ti:sapphire crystal, self-phase modulation and the crucial Kerr-lens mode-locking, which is approximated by a fast saturable absorber *q(z, t)*. By assuming a slowly varying pulse envelope, *A(z, t)* in units of √W, Eq. (1) describes the pulse dynamics with regard to a retarded time frame *t* moving with the group velocity of the pulse.

$$\frac{\partial A(z,t)}{\partial z} = \left[g(z,t) - q(z,t) - j\,\delta\,|\,A(z,t)\,|^2 - j\,\varphi(-j\frac{\partial}{\partial t}) \right] \cdot A(z,t) \qquad (1)$$

$$with\;\; q(z,t) = \frac{q_0}{1 + \dfrac{|\,A(z,t)\,|^2}{P_{Sat}}} \quad and \quad g(z,t) = \frac{g_0}{1 + \dfrac{\int |\,A(z,t)\,|^2\,dt}{W_{Sat}}} \cdot \frac{(\Delta\omega_L)^2}{\omega^2 + (\Delta\omega_L)^2}$$

The complex interplay between the different effects captured by Eq. (1) can be analyzed by applying the Split Step Fourier Method [26] to slices of propagation distance Δz within the crystal (see Fig. 1(b)). To represent the studied laser system appropriately, the parameters were chosen as follows: The self-phase modulation coefficient $\delta = 2\cdot\pi\cdot n_{2,L}/(\lambda\cdot A_{eff})$ with $n_{2,L} = 3\cdot10^{-7}$ (cm^2/W) and λ = 800 nm is determined by the effective beam cross-section A_{eff} in the crystal. Because there is some experimental uncertainty associated with the value of the beam cross-section, (the beam radius was estimated to be 10 μm - 20 μm), we assumed the cross-section so that $\delta = 4\cdot10^{-7}$ $(Wmm)^{-1}$, which agrees with values in [15, 17]. Once a specific A_{eff} for the beam was fixed, the small signal gain and average gain saturation energy were calculated for a ring laser configuration: $W_{Sat,Ring} = h\cdot f_L\cdot A_{eff}/(\sigma\cdot\tau_L\cdot f_{Rep}) = 3.24$ nJ and $g_0 = R_P\cdot\sigma\cdot\tau_L/(2\cdot A_{eff}) = 1.9$ (with *h* Planck's constant, $f_L = 3.75\cdot10^{14}$ Hz, $\sigma = 3\cdot10^{-19}$ cm^2, $\tau_L = 3$ μs, $f_{Rep} = 500$ MHz, $R_P = P_P/(h\cdot f_L) = 6.2$ W/$(h\cdot f_L)$ for the 500 MHz laser, $\Delta\omega_L = 0.24$ rad THz). To obtain stable steady-state pulses with the desired pulse energies, the parameters were slightly adjusted to values of $g_0 = 1.5$ and $W_{Sat,Ring} = 3.35$ nJ in order to simulate the 500 MHz laser.

The saturation power for the saturable absorber was chosen as P_{Sat} = 3 MW. This is equal to about one-third of the pulse peak power in the crystal (compare Fig. 3(a)), so that the saturable absorber is best exploited to form stable pulses (cf. [27]). The modulation depth q_0 of the saturable absorber was set to 5% and represents two to three times the estimated intracavity losses of the laser. This number is justified by the observation that, in order to obtain mode-locking, the laser cavity is initially misaligned with a laser threshold that is two to three times higher than under optimum continuous-wave lasing conditions. Since the threshold for lasing is given by $g_0 > 1 + q_0$ (see [28]), this condition gives an approximate value for the equivalent absorber modulation depth; assuming that, when mode-locked, the laser cavity realigns to maximize output power. As the major pulse shaping effects in the crystal are due to dispersion and self-phase modulation ([15]), gain filtering and saturable absorption largely stabilize the pulse against background radiation and scale the final pulse energy through the combined adjustment of the parameters. Therefore, slight deviations in the latter set of parameters have less effect on the pulse dynamics.

The material dispersion was determined by the refractive index $n(\omega)$, which was obtained from the Sellmeier equations for the different materials [29]. An exception was the refractive index of air, which was calculated by the Edlén formula [30] for a better agreement with the laboratory environment. The spectral phase term $\varphi(\omega)$ for each material incorporates second-order and higher dispersive effects, and is proportional to the actual optical path length of that particular element. In order to include these phase contributions in the free-space section of the laser together with the spectral shaping of the double-chirped mirrors, a spectral transfer function with amplitude $S(\omega)$ and dispersive phase $P(\omega)$ for the linear, passive cavity elements was used. For the ring laser cavity configuration in Fig. 1(a), the pulse propagation outside the crystal is

given by Eq. (2), with $R_{1/2}(\omega)$ denoting the power reflectivity of the DCMs M1 and M2, and $T_{OC}(\omega)$ the transmission of the output coupler (OC) (compare Fig. 2(a) for the 500 MHz ring laser). $A_2(t)$ and $A_9(t)$ represent the pulse amplitude exiting the crystal and after one pass through the remaining passive cavity elements before re-entering the Ti:sapphire crystal, respectively. The dispersive phase $\varphi_i(\omega)$ captures the impact of each mirror (subscript 1 or 2, according to the type of mirror; see Fig. 1(a)) or intracavity material (denoted with the respective material as subscript).

$$\begin{aligned} A_9(\omega) &= S(\omega) \cdot e^{-jP(\omega)} \cdot A_2(\omega) \\ S(\omega) &= \sqrt{R_2(\omega) \cdot R_1(\omega) \cdot T_{OC}(\omega) \cdot R_2(\omega) \cdot R_1(\omega)} \\ P(\omega) &= \varphi_2(\omega) + \varphi_1(\omega) + \varphi_{FS}(\omega) + \varphi_{BaF_2}(\omega) + \varphi_2(\omega) + \varphi_1(\omega) + \varphi_{Air}(\omega) \end{aligned} \tag{2}$$

Fig. 2(c) shows the magnitude S and phase P of the linear passive cavity transfer function versus wavelength for the 500 MHz laser cavity and exemplifies the overall shape of the transfer functions for the examined laser systems. It can be seen that the magnitude S supports the build-up of a broad intracavity spectrum between 640 nm and 1050 nm, while the phase P noticeably incorporates higher order dispersion effects.

Experimental Set-up

The numerical model is applied to laser configurations found in the literature, which are referenced for details: a linear 200 MHz laser [22], a 500 MHz ring laser [21, 23, 24] and a 1 GHz ring laser [25]. Using the 500 MHz ring laser as an example, the important cavity elements in this experimental set-up are explained.

500 MHz ring laser

The experimental set-up of an octave-spanning Ti:sapphire ring laser with a 2-mm-long crystal and a repetition rate of 500 MHz is presented (see Fig. 1(a)). This configuration produces two outputs, a main, carrier-envelope (CE) phase stabilized pulse from the reflective output coupler and a 1f-2f output coupled out through the flat mirror M3, which is used for the detection of the carrier-envelope offset frequency in a 1f-2f interferometer (for details see [24]).

This laser encompasses new, custom-designed DCMs, which were optimized to provide exact compensation of the material dispersion in the cavity while maintaining a smooth phase over a broad wavelength range [31, 32]. Their mirror characteristics are shown in Fig. 2(a): The mirrors labelled M1 and M3 feature a pump window around 532 nm and 50% transmission around 1160 nm and 580 nm, which corresponds to the 1f - 2f frequency components used for carrier-envelope phase stabilization of the laser [33]. Mirrors M2 and M4 are both of the same type and exhibit a high reflectivity over a broader wavelength window to support the build-up of a wide spectrum in the cavity. The group delay for the DCMs in the 500 MHz cavity is illustrated in Fig. 2(b) for the optimized design [31] and the measured mirrors, as determined by white-light interferometry for a normal incidence angle.

In this laser set-up, an output coupler in reflection is used that is coated onto the fused silica wedge. The output coupler has a 2% reflectivity for the main part of the spectrum (Fig. 2(a)). It allows the generation of a broad intracavity spectrum while reflectivities higher than 50% below 590 nm and above 1040 nm effectively enhance and couple out the spectral wings. With such a reflective output coupler, the dispersive phase impact of the OC on the intracavity dispersion is less significant, since the phase in transmission is constrained by Kramers-Kronig relations [34]. Another special component of this laser cavity is the combination of two wedges consisting of fused silica and BaF_2. To fine-tune the intracavity dispersion, the total inserted

material thickness is changed, while at the same time allowing adjustment of the CE phase independently of the intracavity dispersion by interchanging the two materials [35].

Results and Discussion

Pulse Dynamics

According to the dispersion managed mode-locking model, each pulse undergoes significant pulse broadening and compression during each cavity round-trip, depending on the material dispersion encountered in the respective section of the laser. While it is experimentally challenging to determine the actual pulse stretching within the laser cavity, simulations of the intracavity pulse propagation clearly capture the impact of each element on the pulse formation. The numerical analysis follows the temporal and spectral breathing, as demonstrated in Fig. 3, for the 500 MHz laser: Starting at the geometric middle of the Ti:sapphire crystal (label 1 in Fig. 1(b)), the pulse evolution in steady state for one cavity round-trip is displayed in Fig. 3(a): The pulse duration reaches its relative minimum pulse full-width half-maximum in the crystal with 9 fs, which is slightly offset from the geometric middle of the crystal and mostly due to gain filtering and higher order dispersion effects. This minimum pulse duration with its corresponding spectral envelope is determined by interplay among the gain filtering, the chirp of the pulse, and the self-phase modulation, which generates new frequency components, filling up and even exceeding the gain bandwidth. Thus, the strength of the self-phase modulation encountered in the crystal is a major factor that influences the femtosecond pulse generation as the spectrum breathes within the crystal from a FWHM of 50 THz near the center (position 1) to 75 THz (position 2) in Fig. 3(b). While the linear part of the cavity, mainly the mirrors, support the full spectrum, the pulse stretches and compresses according to the dispersion encountered from each

cavity element. Under optimized dispersion compensation achieved through the wedge insertion, the pulse assumes a minimum pulse duration with a peak instantaneous power of ~9 MW at the output coupler (position 5 in Fig. 3(a)), as well as after bouncing off M1 (position 8) before re-entering the crystal again. From a minimum pulse duration of 5.7 fs, it stretches to 53 fs and is recompressed to 32 fs before re-entering the Ti:sapphire crystal.

Output Spectrum

After analyzing the intracavity pulse dynamics, the output spectrum for different laser configurations was examined and the impact of different types of output couplers evaluated: The linear 200 MHz laser has an output coupler in transmission in one of its arms, the 500 MHz laser has an output coupler in reflection, coated on a FS wedge, while the 1 GHz laser essentially uses a flat output coupler by reflecting off a BaF_2 wedge. The goal of the simulations was to predict the spectral bandwidth and shape of the output for comparable pulse energies and average output power (e.g., for the 500 MHz ring laser the average output power from the numerical analysis was 380 mW, which is in accordance with the measured output power of 350 mW [24]). Each displayed power spectral density (PSD) curve in Figs. 4, 5, 6, whether from the experiment or the numerical analysis, is normalized to its maximum amplitude.

In Fig. 4(a) the output spectrum for the linear 200 MHz laser from the experimental set-up and simulation is presented, and the numerical analysis predicts the output spectrum shape accurately. The $ZnSe/MgF_2$ output coupler enhances the wings relative to the main output, and the power transmission for the center wavelengths is 1% (see [22]).

The reflection off the wedge, which generates the main output beam for the 1 GHz ring laser [25], essentially corresponds to the intracavity spectrum, since no spectral shaping occurs by the output coupler. Fig. 4(b) shows the output spectrum and demonstrates how an ultra-

broadband spectrum can be supported within the cavity because of this flat output coupler. A very good agreement between the simulated and measured spectrum on average can be noted, and small substructures occur with the same magnitude in both PSDs. The offset of ~10 nm between certain features in the experiment and the simulation suggests slight differences between the fabricated and the designed mirror data, since the 200 MHz and 1 GHz laser set-ups feature the same mirrors (which are different from the 500 MHz laser). In addition, deviations in the wavelength calibration of the measurement equipment used to characterize this particular laser set-up also explain the slight wavelength offset.

To emphasize the importance of the mirror characteristics, the numerical analysis for the 500 MHz ring laser [23, 24] is conducted with the designed and the experimentally measured mirror data. The difference between the two mirror descriptions is shown in the group delay (GD) of the DCMs, as illustrated in Fig. 2(b). The measured group delay follows the designed group delay closely in the wavelength range of interest (the maximum deviation between both curves for the main part of the spectrum is ±2 fs), but it shows somewhat reduced oscillations in the long-wavelength regime when compared to the design.

The impact of these slight differences in the GD on the spectra can be seen in Figs. 5(a) and 5(b), where the 500 MHz ring laser output spectra for the main output and the 1f-2f referencing beam is shown for three different cases: for simulations using the measured and designed mirror characteristics (i.e., reflectivity and dispersion), and for the experimentally obtained results. The simulated spectra in Figs. 5(a) and 5(b) show good agreement between each other and, on average, good agreement with the measured data. The main features in the spectral wings are accurately reproduced and we can predict the optimized power levels achievable for the 1f and 2f output (with 1160 nm and 580 nm, as 1f and 2f frequencies, illustrated in Fig. 5(b))

on the chosen normalized scale. When comparing the two numerical results for both the 1f-2f output and the main output, the PSD with the designed mirrors falls off slightly steeper in the long-wavelength regime (larger than 1160 nm). As the long wavelengths penetrate deeper into the mirror stacks, they are more prone to fabrication tolerances, which can explain the slight deviations. In addition, the oscillations in the group delay in Fig. 2(b) are more pronounced for the designed DCMs compared to the smoothed measured group delay for long wavelengths. Considering these slight deviations between the designed and measured mirror data, the numerical analysis under two GD conditions predicts stable steady-state outputs, which in both cases compare well with the experimental results. At the same time, incorporating the measured mirror data enhances the agreement between experiment and simulation even further.

Dispersion Compensation

An important factor in optimizing the output spectrum is the overall dispersion compensation in the cavity: Fine-adjustment of the wedge thickness changes the intracavity GDD by a few fs^2 in a very precise fashion and relative changes in the wedge insertion can be determined very accurately in the experimental set-up. To examine the dependence of the spectral wings on the intracavity dispersion, the spectra for small dispersion variations related to changes in the wedge insertion were numerically evaluated. The impact of dispersion fine-adjustment is shown in Fig. 6, where the main output spectrum of the 500 MHz laser is examined for different BaF_2 material thicknesses, while keeping all other parameters constant. The simulated 500 MHz laser was optimized to its broadest, steady-state intracavity spectrum if the cavity contained insertion values of 2.05 mm BaF_2 and 1.84 mm FS, which compare well to the estimated experimental values of 2.07 mm BaF_2 and 1.95 mm FS. For reduced wedge thicknesses, the wings in the spectrum are notably decreased (approximately −12 dB at 1160 nm for small changes in BaF_2

material insertion of only 100 μm, which corresponds to a group delay dispersion of ~4 fs^2 at 800 nm for the 500 MHz ring laser). This is in good agreement with the required experimental fine-tuning of the wedges. At the same time, the sensitivity to the dispersion compensation depends on the actual laser configuration, since the 200 MHz linear laser exhibits approximately −7 dB decrease at 1160 nm for the same relative change in BaF_2 material insertion.

Mirror Ripples

The DCMs are designed in pairs to cancel ripples in the group delay, so that an overall smooth GD is achieved over a broad bandwidth. The impact of the GD ripples on the 200 MHz laser set-up was studied, since the overall mirror oscillations are the most pronounced for this cavity containing 3 DCM pairs: To numerically determine the impact of the GD ripples on an absolute scale itself, the oscillations from the DCMs were extracted and the average GD ripple for each DCM amounted to ~15 fs. These were imposed with certain strengths on each individual mirror in the laser set-up. With stronger GD oscillations in the linear laser (up to double original magnitude, i.e., ripples of ~30 fs), but the same overall net GD at 800 nm, pulse generation was still possible at the cost of reduced pulse energies and smaller maximum instantaneous intensities. For enhanced mirror ripples, the trailing edge of the pulse envelope fell off slower, thus resulting in post-pulses and redistribution of energy into the wings of the pulse. Due to the larger perturbations seen at each mirror reflection, the number of round-trips until the steady state was reached increased by a factor of 2.

Output Pulse

For the 500 MHz ring laser the main output pulse was examined after it was externally compressed by four additional octave-spanning DCMs, a BaF_2 plate, and two thin FS wedges for

fine-dispersion compensation. The transform-limited FWHM pulse duration extracted from the output spectrum could be reduced to 4.2 fs and 3.7 fs, according to simulation and experiment. To evaluate the actual output pulse after compression, the numerical result was compared with the retrieved pulse from two-dimensional spectral shearing interferometry (2DSI) measurements [20, 21, 24], as shown in Fig. 7. The pulse shape and pulse duration of 4.9 fs are exactly reproduced. This result shows that sub-two-cycle pulse generation in Ti:sapphire oscillators can be very well captured with the described one-dimensional temporal model.

Conclusions

We demonstrate that a one-dimensional numerical analysis can accurately describe the laser dynamics of octave-spanning lasers that generate sub-two-cycle pulses for different cavity configurations, by using measured (or designed) mirror dispersion and reflectivity and the dispersion of the other intracavity elements. Our approach shows that the impact of the DCMs and the output coupler on the pulse dynamics and their spectral details are very well captured by this analysis. By optimizing the dispersion compensation and including the experimental device characteristics, we can predict the best achievable performance in terms of output spectrum, the enhancement of spectral wings, and achievable output pulse shape and duration in an actual experimental set-up. Thus, the presented numerical model is a powerful tool for the analysis, design, and optimization of laser components and the general design of octave-spanning lasers.

Acknowledgements

This work was supported in part by Defense Advanced Research Projects Agency (DARPA) grant HR0011-05-C-0155, and AFOSR grant FA9550-07-1-0014. H. M. Crespo acknowledges grant SFRH/BPD/ 27127/2006 from FCT-MCTES, Portugal.

References

1. D. E. Spence, P. N. Kean, W. Sibbett, "60-fsec pulse generation from a self-mode-locked Ti:sapphire laser," Opt. Lett. **16**, 42–44 (1991).
2. R. Ell, U. Morgner, F. X. Kärtner, F. G. Fujimoto, E. P. Ippen, V. Scheuer, G. Angelow, T Schudi, M. J. Lederer, A. Boiko, B. Luther-Davies, "Generation of 5-fs pulses and octave-spanning spectra directly from a Ti:sapphire laser," Opt. Lett. **26**, 373–375 (2001).
3. L. Matos, D. Kleppner, O. Kuzucu, T. R. Schibli, J. Kim, E. P. Ippen, and F. X. Kärtner, "Direct frequency comb generation from an octave-spanning, prismless Ti:sapphire laser," Opt. Lett. **29**, 1683–1685 (2004).
4. S. Rausch, T. Binhammer, A. Harth, J. Kim, R. Ell, F. X. Kärtner, and U. Morgner, "Controlled waveforms on the single-cycle scale from a femtosecond oscillator," Opt. Exp. **16**, 9739-9745 (2008).
5. T. M. Fortier, A. Bartels, S. A. Diddams, "Octave-spanning Ti:sapphire laser with a repetition rate > 1 GHz for optical frequency measurements and comparisons," Opt. Lett. **31**, 1011–1013 (2006).
6. H. A. Haus, "Mode-locking of lasers," IEEE J. Quantum Electron. **6**, 1173–1185 (2000).
7. T. Bravec, Ch. Spielmann, and F. Krausz, "Mode locking in solitary lasers," Opt. Lett. **16**, 1961–1963 (1991).
8. H. A. Haus, J. D. Moores, and L. E. Nelson, "Effect of third order dispersion on passive mode locking," Opt. Lett. **18**, 51–53 (1993).
9. T. Brabec and S. M. J. Kelly, "Third order dispersion as a limiting factor to mode locking in femtosecond solitary lasers," Opt. Lett. **18**, 2002–2004 (1993).

10. I. P. Christov, H. C. Kapteyn, M. M. Murnane, J. Zhou, and C.-P. Huang, "Fourth-order dispersion-limited solitary pulses," Opt. Lett. **19**, 1465–1467 (1994).
11. I. P. Christov, V. D. Stoev, M. M. Murnane, and H. C. Kapteyn, "Mode locking with a compensated space-time astigmatism," Opt. Lett. **20**, 2111–2113 (1995).
12. I. P. Christov, V. D. Stoev, M. M. Murnane, and H. C. Kapteyn, "Sub-10-fs operation of Kerr-lens mode-locked lasers," Opt. Lett. **21**, 1493 (1996).
13. Y. Chen, F. X. Kärtner, U. Morgner, S. H. Cho, H. A. Haus, E. P. Ippen, J. G. Fujimoto, "Dispersion-managed mode locking," J. Opt. Soc. Am. B **16**, 1999–2004 (1999).
14. Y. Chen, H. A. Haus, "Dispersion-managed solitons in the net positive dispersion regime," J. Opt. Soc. Am. B **16**, 24–30 (1999).
15. Q. Quraishi, S. T. Cundiff, B. Ilan, and M. J. Ablowitz, "Dynamics of Nonlinear and Dispersion Managed Solitons," Phys. Rev. Lett. **94**, 243904–243904 (2005).
16. M. V. Tognetti, M. N. Miranda, and H. M. Crespo, "Dispersion-managed mode-locking dynamics in a Ti:sapphire laser," Phys. Rev. A **74**, 033809-1–033809-5 (2006).
17. V. P. Kalosha, M. Müller, J. Herrmann, and S. Gatz, "Spatiotemporal model of femtosecond pulse generation in Kerr-lens mode-locked solid-state lasers," J. Opt. Soc. Am. B **15**, 535–550 (1998).
18. C. Jirauschek, F. Kärtner, and U. Morgner, "Spatiotemporal Gaussian pulse dynamics of Kerr-lens mode-locked lasers," J. Opt. Soc. Am. B **20**, 1356–1368 (2003).
19. C. Jirauschek, U. Morgner, and F. Kärtner, "Variational analysis of spatio-temporal pulse dynamics in dispersive Kerr media," J. Opt. Soc. Am. B **19**, 1716–1721 (2002).
20. J. R. Birge, R. Ell, and F. X. Kärtner, "Two-dimensional spectral shearing interferometry for few-cycle pulse characterization," Opt. Lett. **31**, 2063 – 2065 (2006).

21. M. Y. Sander, H. M. Crespo, J. R. Birge, and F. X. Kärtner, "Modeling of Octave-Spanning Sub-Two-Cycle Titanium:Sapphire Lasers: Simulation and Experiment," Conference on Ultrafast Phenomena, (European Physical Society and Optical Society of America, 2008), paper THUIIIc.
22. O. D. Mücke, R. Ell, A. Winter, J. Kim, J. R. Birge, L. Matos, and F. X. Kärtner, "Self-referenced 200 MHz Octave-Spanning Ti:Sapphire Laser with 50 Attosecond Carrier-Envelope Phase Jitter," Opt. Exp. **13**, 5136–5169 (2005).
23. H. M. Crespo, J. R. Birge, E. L. Falcão-Filho, M. Y. Sander, A. Benedick, and F. X. Kärtner, "Nonintrusive phase stabilization of sub-two-cycle pulses from a prismless octave-spanning Ti:sapphire laser," Opt. Lett., **33**, 833–835 (2008).
24. H. M. Crespo, J. R. Birge, M. Y. Sander, E. L. Falcão-Filho, A. Benedick, and F. X. Kärtner, "Phase stabilization of sub-two-cycle pulses from prismless octave-spanning Ti:sapphire lasers," J. Opt. Soc. Am. B **25**, B147–B154 (2008).
25. A. Benedick, J. Birge, R. Ell, O. D. Mücke, M. Sander, and F. X. Kärtner, "Octave Spanning 1 GHz Ti:sapphire Oscillator for HeNe CH4-based Frequency Combs and Clocks," in CLEO/Europe 2007 (Munich, 17-22 June, 2007), IEEE (2007).
26. G. P. Agrawal, *Nonlinear Fiber Optics* (Academic, 2007).
27. F. X. Kärtner, J. Aus der Au, and U. Keller, "Mode-locking with slow and fast saturable absorbers–what's the difference?" IEEE J. Sel. Top. Quantum Electron. **4**, 159–168 (1998).
28. H. Haus, "Parameter Ranges for CW Passive Mode Locking," IEEE J. Quantum Electron. **12**, 169–176 (1976).
29. Schott Optical Glass Catalog (Schott Glass Technologies Inc., 1992).

30. R. Muijlwijk, “Update of the Edlen’s formulae for the refractive index of air,” Metrologia **25**, 189 (1998).
31. J. R. Birge and F. X. Kärtner, “Efficient optimization of multilayer coatings for ultrafast optics using analytic gradients of dispersion,” Appl. Opt. **46**, 2656–2662 (2007).
32. J. R. Birge and F. X. Kärtner, “Efficient analytic computation of dispersion from multilayer structures,” Appl. Opt. **45**, 1478–1483 (2006).
33. J. R. Birge, H. Crespo, M. Sander, and F. X. Kärtner, “Non-Intrusive Sub-Two-Cycle Carrier-Envelope Stabilized Pulses Using Engineered Chirped Mirrors,” in Conference on Lasers and Electro-Optics/Quantum Electronics and Laser Science conference and Photonic Applications Systems Technologies, 2008, paper CTuC3.
34. G. Lenz, B. J. Eggleton, C. R. Giles, C. K. Madsen, and R. E. Slusher, “Dispersive Properties of Optical Filters for WDM Systems,” IEEE J. Quantum Electron. **34**, 1390 – 1402 (1998).
35. R. Ell, J. R. Birge, M. Araghchini, and F. X. Kärtner, “Carrier-envelope phase control by a composite plate,” Opt. Exp. **14**, 5829–5837 (2006).

List of Figures

Fig. 1: (Color online) (a) Experimental set-up of 500 MHz laser. (b) Schematic model for ring laser used in numerical analysis. The numbering in the ring laser denotes the cavity position used in Fig. 3. (c) Model of linear laser cavity.

Fig. 2: (Color online) (a) DCM reflectivity and output coupler reflectivity for the 500 MHz ring laser. (b) Designed and measured group delay for each type of DCM. The measured data is determined by white-light interferometry at normal incidence angle. (c) Amplitude and phase of linear passive cavity transfer function versus wavelength.

Fig. 3: (Color online) (a) Pulse breathing for the 500 MHz ring laser for one cavity round-trip starting in the geometric middle of the TiSa crystal. (b) Spectral breathing of the power spectral density (PSD) for the 500 MHz ring laser. The position in the cavity labeling refers to Fig. 1(a).

Fig. 4: (Color online) Comparison of the simulated and measured main output spectra: (a) Linear 200 MHz laser, (b) 1 GHz ring laser. Each PSD curve is normalized to its maximum amplitude.

Fig 5: (Color online) (a) Main output spectrum for the 500 MHz ring laser. (b) 1f-2f output spectrum for the 500 MHz ring laser. In both cases the measured spectrum is compared with the simulated output spectra using the designed and experimentally determined DCM data. Each PSD curve is normalized to its maximum amplitude in the center part of the spectrum.

Fig 6: (Color online) Main output spectrum for different dispersion compensation with varying BaF_2 insertion for the 500 MHz laser, normalized to its maximum amplitude. A decrease of 0.1 mm of BaF_2 corresponds to a GD of ~4 fs and a decrease in the spectral wings around 1160 nm of −12 dB.

Fig. 7: (Color online) Output pulse for 500 MHz laser after external compression through a delay line with 2 DCM pairs and FS/BaF_2 material. The measured pulse is retrieved from two-dimensional spectral shearing interferometry (2DSI) measurements and shows excellent agreement with the simulated output pulse.

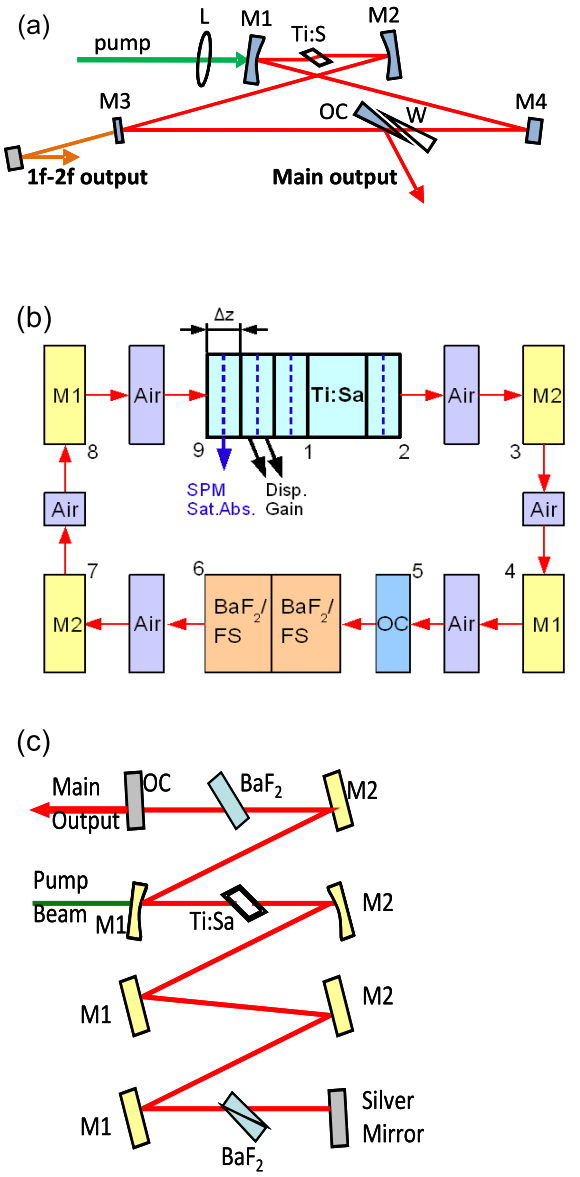

Fig. 1: (Color online) (a) Experimental set-up of 500 MHz laser. (b) Schematic model for ring laser used in numerical analysis. The numbering in the ring laser denotes the cavity position used in Fig. 3. (c) Model of linear laser cavity.

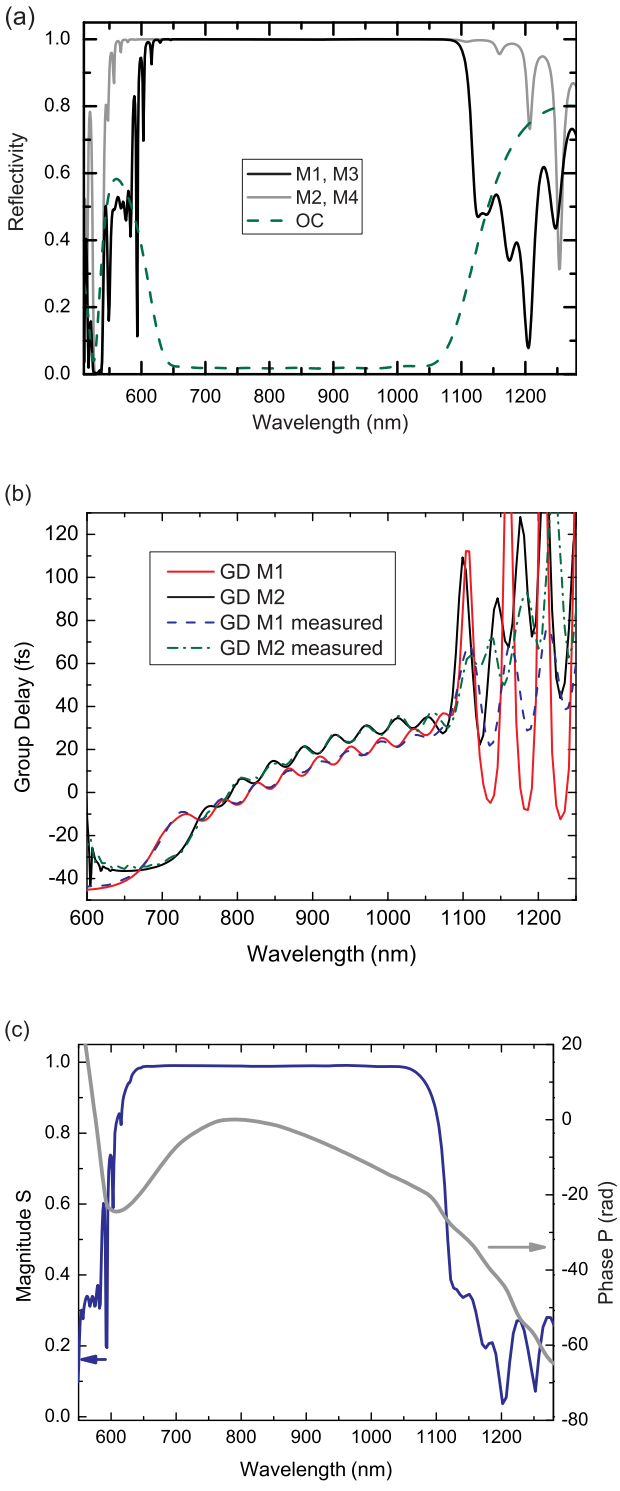

Fig. 2: (Color online) (a) DCM reflectivity and output coupler reflectivity for the 500 MHz ring laser. (b) Designed and measured group delay for each type of DCM. The measured data is

determined by white-light interferometry at normal incidence angle. (c) Amplitude and phase of linear passive cavity transfer function versus wavelength.

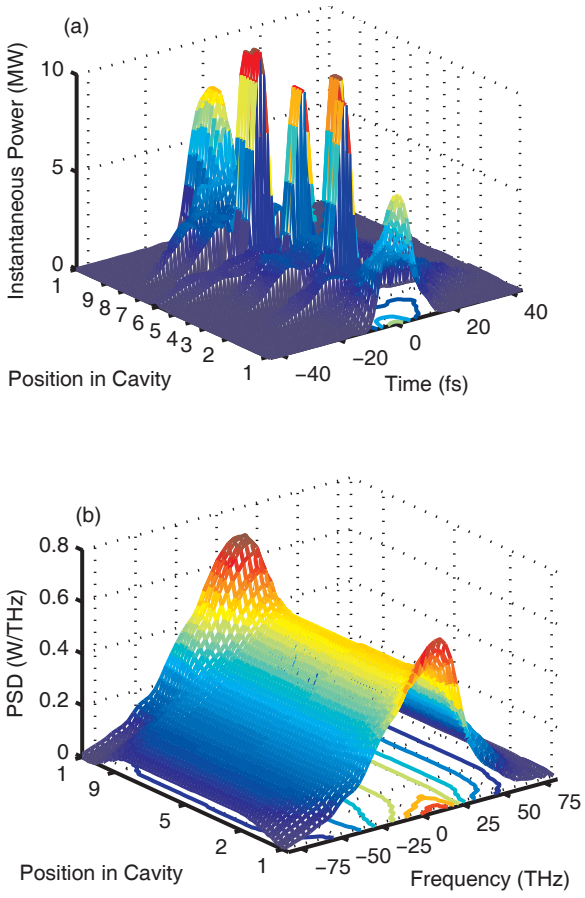

Fig. 3: (Color online) (a) Pulse breathing for the 500 MHz ring laser for one cavity round-trip starting in the geometric middle of the TiSa crystal. (b) Spectral breathing of the power spectral density (PSD) for the 500 MHz ring laser. The position in the cavity labeling refers to Fig. 1(a).

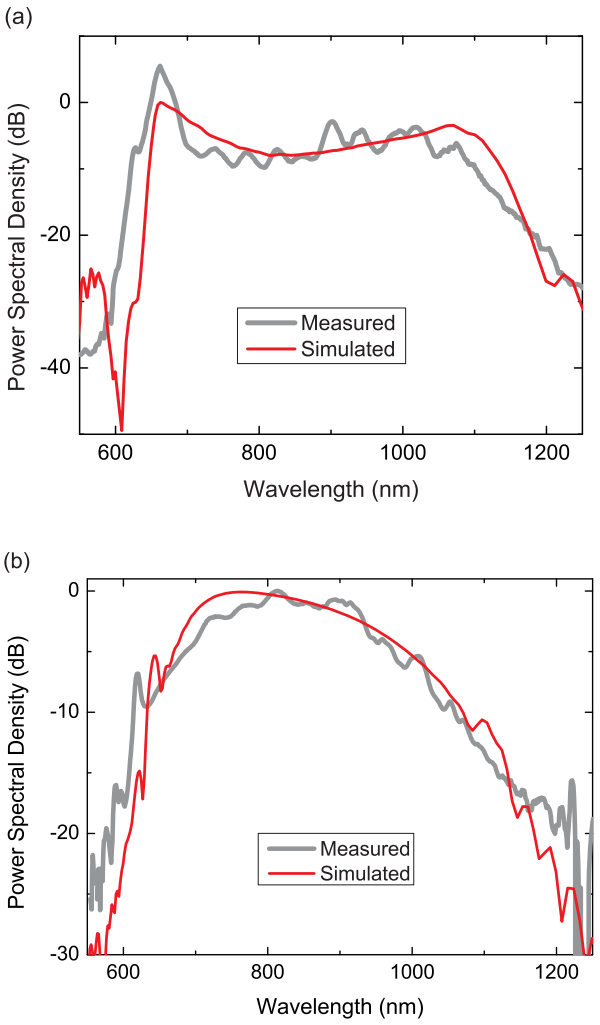

Fig. 4: (Color online) Comparison of the simulated and measured main output spectra: (a) Linear 200 MHz laser, (b) 1 GHz ring laser. Each PSD curve is normalized to its maximum amplitude.

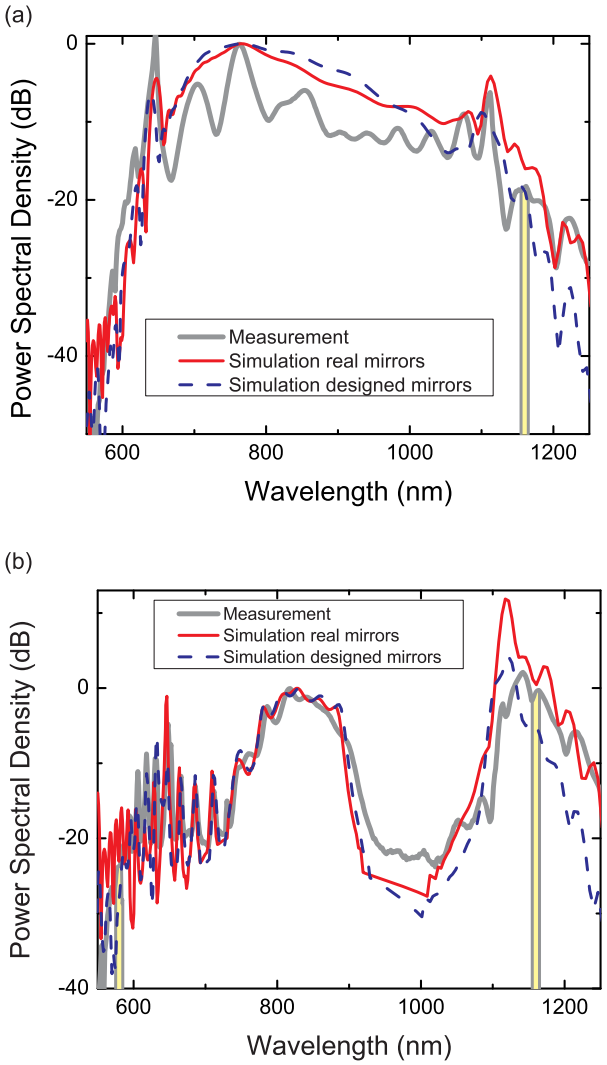

Fig 5: (Color online) (a) Main output spectrum for the 500 MHz ring laser. (b) 1f-2f output spectrum for the 500 MHz ring laser. In both cases the measured spectrum is compared with the simulated output spectra using the designed and experimentally determined DCM data. Each PSD curve is normalized to its maximum amplitude in the center part of the spectrum.

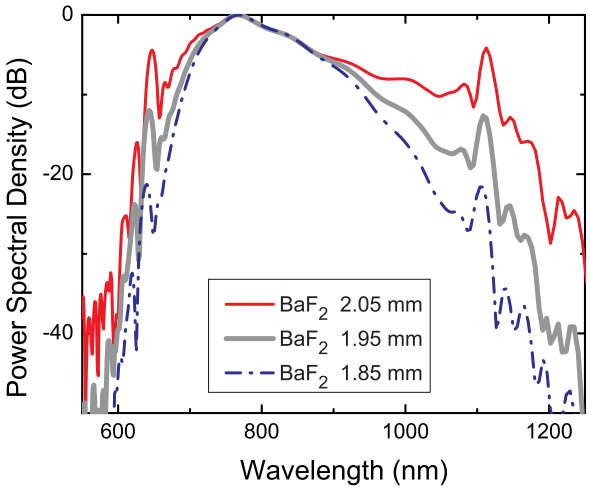

Fig 6: (Color online) Main output spectrum for different dispersion compensation with varying BaF_2 insertion for the 500 MHz laser, normalized to the maximum amplitude. A decrease of 0.1 mm of BaF_2 corresponds to a GD of ~4 fs and a decrease in the spectral wings around 1160 nm of -12 dB.

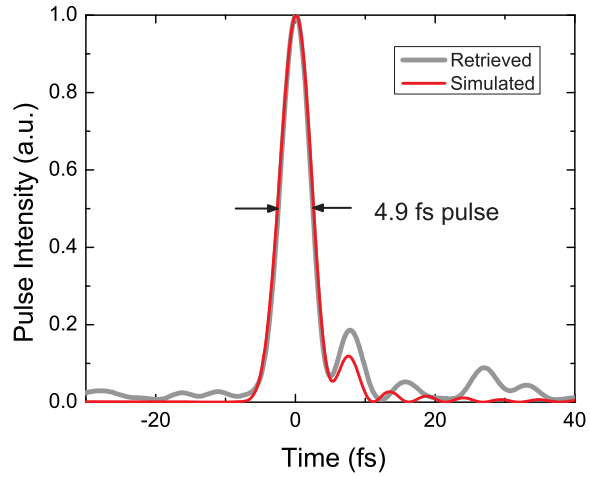

Fig. 7: (Color online) Output pulse for 500 MHz laser after external compression through a delay line with 2 DCM pairs and FS/BaF_2 material. The measured pulse is retrieved from two-dimensional spectral shearing interferometry (2DSI) measurements and shows excellent agreement with the simulated output pulse.